

Biological and Medical Physics, Biomedical Engineering

BIOLOGICAL AND MEDICAL PHYSICS, BIOMEDICAL ENGINEERING

This series is intended to be comprehensive, covering a broad range of topics important to the study of the physical, chemical and biological sciences. Its goal is to provide scientists and engineers with textbooks, monographs, and reference works to address the growing need for information. The fields of biological and medical physics and biomedical engineering are broad, multidisciplinary and dynamic. They lie at the crossroads of frontier research in physics, biology, chemistry, and medicine.

Books in the series emphasize established and emergent areas of science including molecular, membrane, and mathematical biophysics; photosynthetic energy harvesting and conversion; information processing; physical principles of genetics; sensory communications; automata networks, neural networks, and cellular automata. Equally important is coverage of applied aspects of biological and medical physics and biomedical engineering such as molecular electronic components and devices, biosensors, medicine, imaging, physical principles of renewable energy production, advanced prostheses, and environmental control and engineering.

Editor-in-Chief:

Bernard S. Gerstman, Department of Physics, Florida International University, Miami, FL, USA

Editorial Board:

Masuo Aizawa, Department of Bioengineering,
Tokyo Institute of Technology, Yokohama, Japan

Robert H. Austin, Princeton, NJ, USA

James Barber, Wolfson Laboratories, Imperial
College of Science Technology, London, UK

Howard C. Berg, Cambridge, MA, USA

Robert Callender, Department of Biochemistry,
Albert Einstein College of Medicine, Bronx, NY,
USA

George Feher, Department of Physics, University
of California, San Diego, La Jolla, CA, USA

Hans Frauenfelder, Los Alamos, NM, USA

Ivar Giaever, Rensselaer Polytechnic Institute,
Troy, NY, USA

Pierre Joliot, Institute de Biologie Physico-Chi-
mique, Fondation Edmond de Rothschild, Paris,
France

Lajos Keszthelyi, Biological Research Center,
Hungarian Academy of Sciences, Szeged, Hun-
gary

Paul W. King, Biosciences Center and Photobiol-
ogy, National Renewable Energy Laboratory,
Lakewood, CO, USA

Gianluca Lazzi, University of Utah, Salt Lake
City, UT, USA

Aaron Lewis, Department of Applied Physics,
Hebrew University, Jerusalem, Israel

Stuart M. Lindsay, Department of Physics and
Astronomy, Arizona State University, Tempe, AZ,
USA

Xiang Yang Liu, Department of Physics, Faculty
of Sciences, National University of Singapore,
Singapore, Singapore

David Mauzerall, Rockefeller University, New
York, NY, USA

Eugenie V. Mielczarek, Department of Physics
and Astronomy, George Mason University, Fair-
fax, USA

Markolf Niemz, Medical Faculty Mannheim,
University of Heidelberg, Mannheim, Germany

V. Adrian Parsegian, Physical Science Laboratory,
National Institutes of Health, Bethesda, MD, USA

Linda S. Powers, University of Arizona, Tucson,
AZ, USA

Earl W. Prohofsky, Department of Physics, Purdue
University, West Lafayette, IN, USA

Tatiana K. Rostovtseva, NICHD, National Insti-
tutes of Health, Bethesda, MD, USA

Andrew Rubin, Department of Biophysics, Mos-
cow State University, Moscow, Russia

Michael Seibert, National Renewable Energy
Laboratory, Golden, CO, USA


Nongjian Tao, Bidesign Center for Bioelectro-
nics, Arizona State University, Tempe, AZ, USA


David Thomas, Department of Biochemistry,
University of Minnesota Medical School, Min-
neapolis, MN, USA

Michael O. Dada • Bamidele O. Awojoyogbe

Computational Molecular Magnetic Resonance Imaging for Neuro-oncology

 Springer

Michael O. Dada 
Department of Physics
Federal University of Technology
Minna, Nigeria

Bamidele O. Awojoyogbe 
Department of Physics
Federal University of Technology
Minna, Nigeria

ISSN 1618-7210 ISSN 2197-5647 (electronic)
Biological and Medical Physics, Biomedical Engineering
ISBN 978-3-030-76727-3 ISBN 978-3-030-76728-0 (eBook)
<https://doi.org/10.1007/978-3-030-76728-0>

© The Editor(s) (if applicable) and The Author(s), under exclusive license to Springer Nature Switzerland AG 2021

This work is subject to copyright. All rights are solely and exclusively licensed by the Publisher, whether the whole or part of the material is concerned, specifically the rights of translation, reprinting, reuse of illustrations, recitation, broadcasting, reproduction on microfilms or in any other physical way, and transmission or information storage and retrieval, electronic adaptation, computer software, or by similar or dissimilar methodology now known or hereafter developed.

The use of general descriptive names, registered names, trademarks, service marks, etc. in this publication does not imply, even in the absence of a specific statement, that such names are exempt from the relevant protective laws and regulations and therefore free for general use.

The publisher, the authors, and the editors are safe to assume that the advice and information in this book are believed to be true and accurate at the date of publication. Neither the publisher nor the authors or the editors give a warranty, expressed or implied, with respect to the material contained herein or for any errors or omissions that may have been made. The publisher remains neutral with regard to jurisdictional claims in published maps and institutional affiliations.

This Springer imprint is published by the registered company Springer Nature Switzerland AG
The registered company address is: Gewerbestrasse 11, 6330 Cham, Switzerland

Preface

Molecular imaging is promising for two main reasons. First, it enables human diseases to be detected early, that is, before noticeable symptoms manifest. Second, it makes precision drug delivery possible. This technique has the potential of demonstrating changes in tissue physiology, biochemistry, and biology on image scanners. The implication of this is that we can now perform patient-specific treatment, precise follow-up after treatment, and patient monitoring using computational techniques.

Noninvasive medical interventions that effectively increase physician performance in arresting or curing disease, that reduce risk, pain, complications, and reoccurrence for the patient, and that decrease healthcare costs are now within reach. What is yet required is focused reduction of recent and continuing advances in visualization technology to the level of practice, so that they can provide new tools and procedures for smarter healthcare. While magnetic resonance imaging (MRI) is one of the most developed of all the techniques of molecular imaging, it is also unfortunately one of the most expensive diagnostic tools anywhere. It is therefore necessary to develop mathematical concepts based on the fundamental Bloch nuclear magnetic resonance (NMR) flow equation for simple, cost-effective computational MRI to be used in the diagnosis and therapy of brain-related diseases at the molecular level.

The rapid development of innovations including Internet of Things (IoT), big data analysis techniques, and miniature wearable biosensors is generating new opportunities for healthcare systems. Many challenges in the emerging technology can be addressed by the development of consistent, suitable, safe, flexible, and real-time healthcare systems based on the Bloch NMR flow equation.

This book presents mathematical and computational concepts (generally applicable to the analysis of biological and non-biological systems) specifically applied for the analysis of brain tissues and neuro-oncology.

Brain tissues can be likened to complex systems and are often dominated by large numbers of processes. When deviations occur in these processes, human disease conditions are produced. Understanding these processes is important not just in

unraveling the causes of diseases, but also the manner of disease propagation and the best plan for treatment. The inadequate understanding of molecular dynamics of diseases is one reason why many diseases remain incurable and become life-threatening. Molecular MRI now provides new ways of visualizing molecular dynamics and their roles in human diseases.

However, current molecular imaging techniques suffer from low sensitivity as well as problems in temporal and spatial resolutions. The available imaging equipment no longer matches the increasing number of patients requiring diagnosis. The few available imaging machines are costly to maintain while financial difficulties are making acquisition of new ones nigh impossible. Obviously, experimental methods alone are no longer enough for efficient diagnosis, and these challenges may now require development of appropriate mathematical models and sophisticated computer simulations based on the Bloch NMR flow equations to complement laboratory and clinical observations. Such mathematical models have the potential to provide insight into the imaging of the molecular interactions through the analysis of the behavior of relaxation processes as observed on magnetic resonance (MR) scans.

The goal is to explore how patients or hospitals can benefit from using novel situation-aware technologies in real-world settings through the exploitation of big data technologies in the context of smart healthcare: wearable sensors, body area sensors, Internet of Things (IoT), machine learning, and artificial intelligence. Based on this theoretical innovation, it may be possible to develop training software to simulate MRI experiments and provide visual training tools to help understand MRI technology for future generations.

The book is organized as follows. Chapter 1 presents a general introduction to the molecular or cellular processes associated with disease conditions. The development of model solutions to the Bloch NMR flow differential equations which can be applied to describe specific clinical problems is presented in Chap. 2. Chapters 3 and 4 present mathematical analyses developed for radio frequency identification (RFID) systems for computational MRI, based on Bloch NMR flow equations and Hermite functions for detailed studies of processes taking place at molecular level in living tissues (particularly for MRI neuro-oncology).

Chapters 5–10 document analytical expressions obtained for the Bloch NMR flow equations and the solutions developed into the various computer programs used. The nuclei of general interest, hydrogen (proton), and fluorine are very abundant, and they have particularly strong NMR/MRI signals. Hence, Chap. 6 is devoted to quantum and classical mechanical analyses of Bloch NMR flow equations so that the wave function of hydrogen atom and hydrogen-like ions can be represented in terms of NMR/MRI parameters. Chapters 7, 8, and 9 present specific analytical methods and computer programs that may be needed to perform MRI tissue diagnosis and therapy at the molecular level, based on relaxometric data. Chapter 10 focuses on computational analysis of MRI contrast agents and their physico-chemical variables. This is considered very important because of the need to improve the sensitivity and specificity of MR imaging using new MR contrast agents designed to probe specific molecules or cells.

The final chapter, Chap. 11, presents general conclusions.

This book is intended for students, scientists, engineers, medical personnel, and researchers who are interested in developing new concepts for deeper appreciation of computational MRI for medical diagnosis, prognosis, therapy, and management of tissue diseases. Researchers who are interested in developing new concepts for the application of artificial intelligence, machine learning, deep learning, and radiomics to solve real-life biological and medical problems at the molecular level utilizing fundamental mathematical concepts will also find it useful. We hope that this book will help a new generation of researchers who want to be involved in this new field of science which is expected to become of great practical importance. We also expect that this book will provide a new and deeper appreciation of computational MRI.

Minna, Nigeria
Minna, Nigeria

Michael O. Dada
Bamidele O. Awojoyogbe

Acknowledgments

Due to the ability of magnetic resonance imaging (MRI) to probe right to the fundamental level, scientists may be able to image human cellular functions and such imaging modalities would definitely help in the understanding of human disease conditions and thus permit the physician to make more specific diagnosis, prognosis, and the appropriate therapy. The basic challenge in this direction is finding the right mathematical frameworks and the physics which appropriately describe the processes involved. This book was written to meet this challenge. Particularly essential to the development of the initial concepts of the book were the research meetings and seminars as well as the symposia, workshops, conferences, schools, and colleges held at the International Center for Theoretical Physics (ICTP), Trieste, Italy, that Awojoyogbe attended as an ICTP regular associate between the year 2000 and 2008. We would like to take this opportunity to thank the following senior academics: Professor D. K. De of Sustainable Green Power Technologies, USA, Professor P. Boesiger of the Institute of Biomedical Engineering and Medical Informatics, University and ETH, Zurich, Switzerland, Professor Paola Fantazzini of the University of Bologna, Italy, Professor Silvio Aime of University of Torino, Italy, Professor Bill Price of Western Sydney University, Australia, and Professor Julian Chela-Flores of ICTP, Trieste, Italy, for their academic guidance and encouragement. We thank Dr. Udunna Anazodo of Western University, Canada, for her determination to promote MRI training and research among younger scientists. We would like to thank our immediate past and present Vice Chancellors of our University: Professor M. A. Akanji and Professor Abdullahi Bala for providing the needed academic leadership and encouragement. We appreciate Professor Funmi O. Olubode-Sawe of Federal University of Technology, Akure, for her support on English language editing of this book. We thank the unanimous reviewers of this book and the editorial team of the distinguished Biological and Medical Physics/Biomedical Engineering series of Springer Nature for supporting the publication of this book. Finally, we thank the students, scientists, engineers, medical personnel, researchers, and research administrators from all over the world who are interested in reading this book for developing new concepts for

deeper appreciation of computational MRI for medical diagnosis, prognosis, therapy, and management of tissue diseases.

Kindly send your feedback to us through abamidele@futminna.edu.ng or awojoyogbe@yahoo.com.

Contents

1	General Introduction	1
1.1	Molecular or Cellular Processes Associated with Disease Conditions	1
1.2	Molecular Imaging	3
1.3	Importance of Molecular Imaging in Human Medicine	4
1.4	Molecular Imaging Techniques	5
1.5	Significance of MRI Techniques	8
2	Fundamental Physics of Nuclear Magnetic Resonance	11
2.1	Overview of Magnetic Resonance Imaging	11
2.1.1	Principles of Magnetic Resonance Imaging	12
2.1.2	Physics of Magnetic Resonance Imaging	14
2.1.3	Magnetic Resonance Imaging Equipment	15
2.1.4	Image Acquisition and Computation	16
2.1.5	Image Contrast	16
2.1.6	Applications of MR Imaging	17
2.2	MR Contrast Agents and Their Physicochemical Basis	19
2.2.1	Methods of Generating Contrast in MR Agents	20
2.2.2	Atomic Basis of Magnetic Resonance	21
2.2.3	Relaxivity and T_1 , T_2 , T_2^* Contrast Agents	22
2.2.4	Chemistry of T_1 Agents	24
2.2.5	T_2 Agents	25
2.2.6	Functionalization of MR Contrast Agents	26
2.3	Principles of Optics in Magnetic Resonance	29
2.3.1	Bloch Equations in Optics	30
2.4	Computational Science	30
2.4.1	Computational Science and Problem Solving	31
2.4.2	Advantages of Computational Model	33
2.5	Compressed Sensing MRI and Computational Science	34
2.6	MRI in Molecular Imaging	35

- 2.7 Theoretical Treatment of Magnetic Resonance 37
 - 2.7.1 Theoretical Background of Magnetic Resonance 37
 - 2.7.2 The Bloch Equations 45
 - 2.7.3 Quantum and Classical Descriptions of Spin Motion 67
 - 2.7.4 Quantum Treatment of NMR Relaxation 71
 - 2.7.5 Modelling and Differential Equations
in Computational MRI 90
 - 2.7.6 Formulation of the Bloch Equations for Treatment
of Fluids in Motion 91
 - 2.7.7 Diffusion Process in Magnetic Resonance 99
 - 2.7.8 Advection–Diffusion in Nuclear Magnetic
Resonance 103
 - 2.7.9 Justification for Assumption of the Nature
of Transverse Magnetization 107
 - 2.7.10 Variable Fluid Flow Corrections to the Bloch
NMR Flow Equation 108
- 3 Radiofrequency Identification System for Computational
Diffusion Magnetic Resonance Imaging Based on Bloch’s
NMR Flow Equation and Hermite Functions 115**
 - 3.1 Introduction 115
 - 3.2 Mathematical Analysis 118
 - 3.3 Development of Non-gradient MRI 123
 - 3.4 A New Method for Diffusion MRI 125
 - 3.5 Computational Analysis 128
 - 3.6 Discussion 135
 - 3.7 Conclusion 137
- 4 Radio-Frequency Identification System for Computational
Magnetic Resonance Imaging of Blood Flow at Suction Points 139**
 - 4.1 Introduction to Blood Flow and MRI 139
 - 4.2 Analytical Method 140
 - 4.3 Analysis of Blood Flow at Suction Points 146
 - 4.4 Computational Analysis of Blood Flow at Suction Points 149
 - 4.5 RF ID and Velocity Data Generation for Different Tissues 166
 - 4.6 Conclusion 166
- 5 A Computational MRI Based on Bloch’s NMR Flow
Equation, MRI Fingerprinting and Python Deep Learning
for Classifying Adult Brain Tumors 179**
 - 5.1 Introduction 179
 - 5.2 Computational Modelling of the Bloch NMR
Flow Equation 181
 - 5.3 Relaxometry Data 182
 - 5.4 Computation of Magnetic Resonance Signal Dataset 183
 - 5.5 Data Visualization 183

5.6	Linear Regression	183
5.7	Machine Learning	191
5.7.1	Logistic Regression	191
5.7.2	Support Vector Machine	202
5.7.3	Naive Bayes	202
5.7.4	Decision Tree	202
5.7.5	Random Forest	204
5.7.6	Extra Trees	204
5.7.7	K Nearest Neighbors	204
5.7.8	XGBoost	204
5.8	Shallow Deep Learning	205
5.9	Deep Neural Network	205
5.10	Discussions	210
5.11	Conclusion	210
6	Analysis of the Hydrogen-Like Atom for Neuro-Oncology Based on Bloch’s NMR Flow Equation	219
6.1	Background to Quantum Mechanical Treatment of Bloch Flow Equation	219
6.2	Quantum Mechanical Understanding of Classical NMR/MRI	220
6.3	Mathematical Representation of NMR/MRI in Quantum Mechanical Domain	221
6.4	Formulation of the Yukawa Potential for NMR Wave Equation	223
6.5	Formulation of the Coulomb Potential for NMR Wave Equation	231
6.6	Quantum Neuro-Oncology	237
6.7	Analysis of Radiofrequency Pulse as a Function of Radial Distance of the Atoms	240
6.8	Discussion	241
6.9	Conclusion	246
7	Quantum Mechanical Model of the Bloch NMR Flow Equations for Transport Analysis of Quantum-Drugs in Microscopic Blood Vessels Applicable in Nanomedicine	247
7.1	Introduction	247
7.2	Quantum Mechanical Model of Bloch NMR Flow Equations	248
7.3	Application to Nanotechnology	251
7.4	Quantum Drugs Model	252
7.5	Application of the WKB Approximation	254
7.6	The Tunnelling Effect of Quantum Drugs	257
7.7	Description of QM-Designed Drugs in Protein-Structured Nanomachines	264
7.8	Conclusion	265

8	Application of “R” Machine Learning for Magnetic Resonance Relaxometry Data Representation and Classification of Human Brain Tumours	269
8.1	Introduction	269
8.2	Dataset of NMR Relaxometry for Three Classes of Brain Tumor	276
8.3	Statistical Summary of the MRI Relaxometry Dataset	280
8.4	Visualization of the MRI Relaxometry Dataset	281
8.5	Model Construction	283
8.6	Model Prediction	286
8.7	Discussion of Results	287
8.8	Conclusion	288
9	Advanced Magnetic Resonance Image Processing and Quantitative Analysis in Avizo for Demonstrating Radiomic Contrast Between Radiation Necrosis and Tumor Progression	289
9.1	Potential Application of Radiomics	289
9.2	Factors Affecting Radiomic Feature Quantification	290
9.3	Machine Learning in Radiomics	290
9.4	Semi-Supervised Learning	290
9.5	Deep Learning	291
9.6	Research Opportunities and Challenges	291
9.7	Procedures in Advanced Image Processing and Quantitative Analysis	291
9.7.1	Processing Grayscale Images in Avizo	292
9.7.2	Interpretation as 2D Image or 3D Stack	293
9.7.3	Binarization of Grayscale Images	294
9.7.4	Image Separation	295
9.7.5	Image Analysis	298
9.7.6	Extracted Numerical Data	298
9.7.7	Visualizations of Extracted Data	299
9.7.8	Interactive Selection of the Data	299
9.8	Image-Based Filtering	301
9.9	Discussion	307
9.10	Conclusion	309
10	Computational Analysis of Magnetic Resonance Imaging Contrast Agents and Their Physico-Chemical Variables	313
10.1	Analytical Method for Monitoring the Dynamics of Responsive Contrast Agents	313
10.2	Bloch NMR Flow Model for Contrast Agents Moving in 1 D Tissue Spaces	314
10.3	Application of Model to Cardiovascular Disease	316

- 10.4 Computational Monitoring the Dynamics of Contrast Agents . . . 316
- 10.5 Computational Model for Comparative Analysis
of MRI Contrast Agents 318
- 10.6 Development of Machine Learning Classification
Algorithm for Screening MRI Contrast Agents 323
 - 10.6.1 Data Preparation 325
 - 10.6.2 Data Visualization 327
 - 10.6.3 XGBoost Model for Classification 328
- 10.7 Bridging the Gap Between Computational Models and
Experimental Imaging 337
- 10.8 Discussion 342
- 10.9 Conclusion 345
- 11 General Conclusion 347**
- Bibliography 351**
- Index 377**

List of Figures

Fig. 2.1	Scientific fields influencing computational science	32
Fig. 2.2	Processes involved in mathematical model generation and their inter-relationships	33
Fig. 2.3	Illustration of the Larmor precession of the magnetization vector M about the static magnetic field B_0	42
Fig. 2.4	The concept of the rotation of a primed reference frame in which a magnetic moment is at rest	46
Fig. 2.5	Local magnetic field in (a) laboratory frame (b) rotating frame	50
Fig. 2.6	Magnetization vector (a) precessing about the effective field (b) precessing in the $x - y$ plane	51
Fig. 3.1	Profile of ω_1^{RFID} across the range of T_1 in normal brain tissues	129
Fig. 3.2	Profile of ω_1^{RFID} across the range of T_2 in normal brain tissues	130
Fig. 3.3	Profile of ω_1^{RFID} across the range of T_1 for three tumor types found in a solid tumor region	130
Fig. 3.4	Profile of ω_1^{RFID} across the range of T_2 for three tumor types found in a solid tumor region	130
Fig. 3.5	Profile of ω_1^{RFID} across the range of T_1 for three tumor types found in peritumoral white matter region	131
Fig. 3.6	Profile of ω_1^{RFID} across the range of T_2 for three tumor types found in peritumoral white matter region	131
Fig. 3.7	Profile of ω_1^{RFID} across the range of T_1 for three tumor types found in contralateral white matter region	132
Fig. 3.8	Profile of ω_1^{RFID} across the range of T_2 for three tumor types found in contralateral white matter region	132

Fig. 3.9 MR transverse magnetization distribution across T_1 and T_2 relaxation times for (a) Frontal white matter (b) Corpus callosum genu (c) Corpus callosum splenium (d) Occipital white matter (e) Frontal gray matter (f) Occipital gray matter (g) Caudate (h) Putamen (i) Thalamus 133

Fig. 3.10 MR transverse magnetization distribution across T_1 and T_2 relaxation times in solid tumor for (a) glioblastoma multiforme (b) metastasis (c) low grade glioma 134

Fig. 3.11 MR transverse magnetization distribution across T_1 and T_2 relaxation times in peritumoral white matter for (a) glioblastoma multiforme (b) metastasis (c) low grade glioma 134

Fig. 3.12 MR transverse magnetization distribution across T_1 and T_2 relaxation times in contralateral white matter for (a) glioblastoma multiforme (b) metastasis (c) low grade glioma 135

Fig. 3.13 Reconstructed (a) diffusion weighted image with $b = 0$ (b) diffusion weighted image with $b = 8000 \text{ s/mm}^2$ (c) angular frequency image, using the extracted data 137

Fig. 4.1 The asymptotic profile in uniform suction of a fluid flow model for $\lambda = 0$ and $\lambda \ll 1$ 146

Fig. 4.2 Plots of NMR transverse magnetization within the plates as shown in Fig. 4.1 for different capture velocities (depicted by n) and parameter $a = 1$ at suction parameter (a) $\lambda = 0.001$ (b) $\lambda = 0.01$ (c) $\lambda = 0.1$ (d) $\lambda = 1$ 149

Fig. 4.3 Plots of NMR transverse magnetization within the plates as shown in Fig. 4.1 for different capture velocities (depicted by n) and parameter $a = 5$ at suction parameter (a) $\lambda = 0.001$ (b) $\lambda = 0.01$ (c) $\lambda = 0.1$ (d) $\lambda = 1$ 150

Fig. 4.4 Plots of NMR transverse magnetization within the plates as shown in Fig. 4.1 for different capture velocities (depicted by n) and parameter $a = 10$ at suction parameter (a) $\lambda = 0.001$ (b) $\lambda = 0.01$ (c) $\lambda = 0.1$ (d) $\lambda = 1$ 150

Fig. 4.5 Plots of NMR transverse magnetization within the plates as shown in Fig. 4.1 for different capture velocities (depicted by n) and parameter $a = 15$ at suction parameter (a) $\lambda = 0.001$ (b) $\lambda = 0.01$ (c) $\lambda = 0.1$ (d) $\lambda = 1$ 151

Fig. 4.6 Plots of NMR transverse magnetization within the plates as shown in Fig. 4.1 for different capture velocities (depicted by n) and parameter $a = 20$ at suction parameter (a) $\lambda = 0.001$ (b) $\lambda = 0.01$ (c) $\lambda = 0.1$ (d) $\lambda = 1$ 151

Fig. 4.7 Plots of NMR transverse magnetization within the plates as shown in Fig. 4.1 for different capture velocities (depicted by n) and parameter $a = 25$ at suction parameter (a) $\lambda = 0.001$ (b) $\lambda = 0.01$ (c) $\lambda = 0.1$ (d) $\lambda = 1$ 152

Fig. 4.8 Plots of NMR transverse magnetization within the plates as shown in Fig. 4.1 for different capture velocities (depicted as n) and parameter $a = 50$ at suction parameter (a) $\lambda = 0.001$ (b) $\lambda = 0.01$ (c) $\lambda = 0.1$ (d) $\lambda = 1$ 152

Fig. 4.9 Plots of NMR transverse magnetization within the plates as shown in Fig. 4.1 for different capture velocities (depicted as n) and parameter $a = 0.1$ at suction parameter (a) $\lambda = 0.001$ (b) $\lambda = 0.01$ (c) $\lambda = 0.1$ (d) $\lambda = 1$ 153

Fig. 4.10 Plots of NMR transverse magnetization within the plates as shown in Fig. 4.1 for difference capture velocities (depicted as n) and parameter $a = 0.01$ at suction parameter (a) $\lambda = 0.001$ (b) $\lambda = 0.01$ (c) $\lambda = 0.1$ (d) $\lambda = 1$ 153

Fig. 4.11 Plots of NMR transverse magnetization within the plates as shown in Fig. 4.1 for different capture velocities (depicted as n) and parameter $a = 0.001$ at suction parameter (a) $\lambda = 0.001$ (b) $\lambda = 0.01$ (c) $\lambda = 0.1$ (d) $\lambda = 1$ 154

Fig. 4.12 Plots of NMR transverse magnetization within the plates as shown in Fig. 4.1 at suction parameter $\lambda = 0.1$ with parameter $a = 0.0001$ for difference capture velocities (a) $n = 0$ (b) $n = 1$ (c) $n = 2$ (d) $n = 3$ (e) $n = 4$ (f) $n = 5$ 155

Fig. 4.13 Density plots of NMR transverse magnetization against $h = y$ (within the plates) and capture parameter a at suction parameter $\lambda = 0.001$ for velocity parameters (a) $n = 0$ (b) $n = 1$ (c) $n = 2$ (d) $n = 3$ (e) $n = 4$ (f) $n = 5$ 158

Fig. 4.14 Density plots of NMR transverse magnetization against $h = y$ (within the plates) and capture parameter a at suction parameter $\lambda = 0.01$ for velocity parameters (a) $n = 0$ (b) $n = 1$ (c) $n = 2$ (d) $n = 3$ (e) $n = 4$ (f) $n = 5$ 159

Fig. 4.15 Density plots of NMR transverse magnetization against $h = y$ (within the plates) and capture parameter a at suction parameter $\lambda = 0.1$ for velocity parameters (a) $n = 0$ (b) $n = 1$ (c) $n = 2$ (d) $n = 3$ (e) $n = 4$ (f) $n = 5$ 160

Fig. 4.16 Density plots of NMR transverse magnetization against $h = y$ (within the plates) and capture parameter a at suction parameter $\lambda = 1$ for velocity parameters (a) $n = 0$ (b) $n = 1$ (c) $n = 2$ (d) $n = 3$ (e) $n = 4$ (f) $n = 5$ 161

Fig. 4.17 Density plots of NMR transverse magnetization against $h = y$ (within the plates) and λ at capture parameter $a = 0.01$ for velocity parameters (a) $n = 0$ (b) $n = 1$ (c) $n = 2$ (d) $n = 3$ (e) $n = 4$ (f) $n = 5$ 162

Fig. 4.18 Density plots of NMR transverse magnetization against $h = y$ (within the plates) and λ at capture parameter $a = 0.1$ for velocity parameters (a) $n = 0$ (b) $n = 1$ (c) $n = 2$ (d) $n = 3$ (e) $n = 4$ (f) $n = 5$ 163

Fig. 4.19	Density plots of NMR transverse magnetization against $h = y$ (within the plates) and λ at capture parameter $a = 1$ for velocity parameters (a) $n = 0$ (b) $n = 1$ (c) $n = 2$ (d) $n = 3$ (e) $n = 4$ (f) $n = 5$	164
Fig. 4.20	Density plots of NMR transverse magnetization against $h = y$ (within the plates) and λ at capture parameter $a = 10$ for velocity parameters (a) $n = 0$ (b) $n = 1$ (c) $n = 2$ (d) $n = 3$ (e) $n = 4$ (f) $n = 5$	165
Fig. 5.1	Correlation matrices of features in the dataset of (a) Table 5.2, (b) Table 5.3	192
Fig. 5.2	Linear regression plots of T_1 against T_2 using the datasets of (a) Table 5.2, (b) Table 5.3	193
Fig. 5.3	Linear regression plots of T_0 against (a) transverse magnetization, (b) MR signal using the datasets of Tables 5.2 and 5.3	194
Fig. 5.4	Box plots showing maximum, minimum and the median values of T_1 using the datasets of (a) Table 5.2, (b) Table 5.3	203
Fig. 5.5	Profile of the training accuracy of a shallow neural network executed on the datasets of (a) Table 5.2, (b) Table 5.3	206
Fig. 5.6	Profile of the training loss of a shallow neural network executed on the datasets of (a) Table 5.2, (b) Table 5.3	207
Fig. 5.7	Profile of the training accuracy of a deep neural network executed on the datasets of (a) Table 5.2, (b) Table 5.3	208
Fig. 5.8	Profile of the training loss of a deep neural network executed on the datasets of (a) Table 5.2, (b) Table 5.3	209
Fig. 5.9	Scatter plots of T_1 against T_2 for the dataset of (a) Table 5.2, (b) Table 5.3	211
Fig. 5.10	Scatter plots of T_0 against (a) transverse magnetization, (b) NMR signal using the data sets of Tables 5.2 and 5.3	212
Fig. 5.11	Box plots showing maximum, minimum and the median values of T_2 using the datasets of (a) Table 5.2, (b) Table 5.3	213
Fig. 5.12	Box plots showing maximum, minimum and the median values of T_0 using the datasets of (a) Table 5.2, (b) Table 5.3	214
Fig. 5.13	Box plots showing maximum, minimum and the median values of (a) transverse magnetization, (b) MR signal using the datasets of Tables 5.2 and 5.3	215
Fig. 5.14	Andrew curves for the datasets of (a) Table 5.2, (b) Table 5.3	216
Fig. 6.1	NMR transverse magnetization profiles of cytochrome C molecule under the influence of Yukawa potential for (a) 1s, (b) 2s, (c) $2p_x$, (d) $2p_y$, (e) 3s, (f) $3p_x$ orbitals	239

Fig. 6.2	NMR transverse magnetization profiles of cytochrome C molecule under the influence of Coulomb potential for (a) 1s, (b) 2s, (c) 2p _x , (d) 2p _y , (e) 3s, (f) 3p _x orbitals	240
Fig. 6.3	Plots of particle energy in the presence of Yukawa potential as a function of energy level at different angular momentum states	243
Fig. 6.4	Plots of particle energy in the presence of Coulomb potential as a function of energy level at different values of ζ	244
Fig. 6.5	Profiles of applied radiofrequency in the presence of Yukawa potential ($\zeta = 700$) for (a) reduced cytochrome C, (b) oxidized cytochrome C	244
Fig. 6.6	Profiles of applied radiofrequency in the presence of Coulomb potential ($\zeta = 500$) for (a) reduced cytochrome C, (b) oxidized cytochrome C	245
Fig. 7.1	2D profiles of NMR transverse magnetization for different types of human blood vessels at energy level, $n = 1$	253
Fig. 7.2	Contour profiles of NMR transverse magnetization for different types of human blood vessels ($D = 500$)	258
Fig. 7.3	2D profiles of NMR transverse magnetization for different types of human blood vessels ($D = 500$)	258
Fig. 7.4	A typical barrier potential from human heart with quantum drug(s) motion from region I to region III nearly impossible. (Adapted from https://www.labroots.com/trending/cardiology/2335/preventing-heart-failure-after-acute-myocardial-infarction)	260
Fig. 7.5	Plots of the transmission coefficient TC against V_{II} and potential $\omega_{I,II}$ based on Eq. (7.59) for barrier width of (a) 2.5 nm, (b) 3.5 nm, (c) 5.5 nm, (d) 10.5 nm	261
Fig. 7.6	Plots of the transmission coefficient TC against $\omega_{I,II}$ and the barrier width for (a) $E < V_{II}$ ($V_I = 2.6$ mJ, $V_{II} = 11.2$ mJ), (b) $E = V_{II}$ ($V_I = 2.6$ mJ, $V_{II} = 10.8$ mJ), (c) $E > V_{II}$ ($V_I = 2.6$ mJ, $V_{II} = 4.5$ mJ), (d) $E > V_{II} < V_I$ ($V_I = 2.6$ mJ, $V_{II} = 1.2$ mJ)	262
Fig. 7.7	Contour profiles of NMR transverse magnetization for different types of human blood vessels	265
Fig. 7.8	2D profiles of NMR transverse magnetization for different types of human blood vessels at energy level, $n = 2$	266
Fig. 7.9	Plots of the Fourier transform of NMR transverse magnetization for different types of human blood vessels at both linear and log scales ($D = 5 \times 10^{24}$)	267
Fig. 8.1	Boxplot of each NMR relaxation features	281
Fig. 8.2	Boxplot of each NMR relaxation features according to tumour type	282

Fig. 8.3 Probability density plots of the NMR relaxation features 282

Fig. 8.4 Correlation matrix of the dataset 283

Fig. 8.5 Plots of the model evaluation results 285

Fig. 9.1 T2-weighted FLAIR magnetic resonance imaging showing (a) progressive tumour, (b) radiation necrosis (Mehrabian et al., 2017) 292

Fig. 9.2 Removal of noise from the necrosis image using median filter 293

Fig. 9.3 Interactive thresholding on the necrosis image 294

Fig. 9.4 Interactive thresholding on the tumor image 295

Fig. 9.5 Binary image of necrosis displayed with OrthoSlice 296

Fig. 9.6 Binary image of tumor displayed with an OrthoSlice 296

Fig. 9.7 Necrosis image component separation 297

Fig. 9.8 Tumor image component separation 297

Fig. 9.9 Bar chart of necrosis image data 303

Fig. 9.10 Bar chart of tumor image data 304

Fig. 9.11 Plot of the area against image elements (index) for radiation necrosis and tumour progression 304

Fig. 9.12 Plot of the BaryCenterX against image elements (index) for radiation necrosis and tumour progression 304

Fig. 9.13 Plot of the BaryCenterY against image elements (index) for radiation necrosis and tumour progression 305

Fig. 9.14 3D plot of area against BaryCenterX and BaryCenterY for tumour progression image 305

Fig. 9.15 3D plot of area against BaryCenterX and BaryCenterY for radiation necrosis image 306

Fig. 9.16 Interactive selection of necrosis image 306

Fig. 9.17 Interactive selection of tumor image 307

Fig. 9.18 Reconstruction of necrosis image from filtered data 307

Fig. 9.19 Reconstruction of tumor image from filtered data 308

Fig. 9.20 Filtered extracted data bar chart for radiation necrosis 308

Fig. 9.21 Filtered extracted data bar chart for tumour progression 309

Fig. 9.22 3D plot of area against BaryCenterX and BaryCenterY for radiation necrosis image using filtered data 310

Fig. 9.23 3D plot of area against BaryCenterX and BaryCenterY for tumour progression image using filtered data 310

Fig. 9.24 Plot of the filtered area against image elements (index) for radiation necrosis and tumour progression 312

Fig. 9.25 Plot of the filtered BaryCenterX against image elements (index) for radiation necrosis and tumour progression 312

Fig. 9.26 Plot of the filtered BaryCenterY against image elements (index) for radiation necrosis and tumour progression 312

Fig. 10.1 (a–d) Contour profiles of contrast agent concentration as a function of the transverse magnetisation and x using relaxation parameters of human blood at 1.5 T for various spatial resolutions 317

Fig. 10.2 Contour profiles of concentration as a function of transverse magnetisation and x using relaxation properties of human blood at 1.5 T and hemodynamic properties of (a) aorta (b) artery (c) arteriole (d) capillary 318

Fig. 10.3 Graphic user interface of the simulation computer program 321

Fig. 10.4 Profiles of spatial variations of M_y determined from relaxivity values measured in the blood for (a) Magnevist (b) Gadovist (c) Prohance (d) Multihance 322

Fig. 10.5 Profiles of spatial variations of M_y determined from relaxivity values measured in plasma for (a) Magnevist (b) Gadovist (c) Prohance (d) Multihance 324

Fig. 10.6 Profiles of spatial variations of M_y determined from relaxivity values measured in water for (a) Magnevist (b) Gadovist (c) Prohance (d) Multihance 326

Fig. 10.7 r_1 relaxivity distribution for selected contrast agents 333

Fig. 10.8 r_2 relaxivity distribution for selected contrast agents 334

Fig. 10.9 Correlation matrix of the dataset of (a) r_1 (b) r_2 relaxivities 335

Fig. 10.10 Confusion matrix from XGBClassifier for (a) r_1 relaxivity (b) r_2 relaxivity 336

Fig. 10.11 Reconstructed (a) precontrast image (b) postcontrast image at 1 min (c) postcontrast image at 10 min, of small hemangioma in a 53 years old man 338

Fig. 10.12 Reconstructed (a) precontrast image (b) postcontrast image at 1 min (c) postcontrast image at 10 min, of medium-sized hemangioma in a 43 years old man 339

Fig. 10.13 Reconstructed (a) precontrast image (b) postcontrast image at 1 min (c) postcontrast image at 10 min, of large hemangioma in a 51 years old woman 340

Fig. 10.14 Reconstructed (a) postcontrast concentration image at 1 min (b) postcontrast concentration image at 10 min image, of small hemangioma in a 53 years old man 342

Fig. 10.15 Reconstructed (a) postcontrast concentration image at 1 min (b) postcontrast concentration image at 10 min image, of medium-sized hemangioma in a 43 years old man 343

Fig. 10.16 Reconstructed (a) postcontrast concentration image at 1 min (b) postcontrast concentration image at 10 min image, of large hemangioma in a 53 years old woman 344

Fig. 11.1 Workflow of radiomics in neuro-oncology and their relationship to the Bloch NMR flow equation and RF excitation 348

List of Tables

Table 1.1	Medical imaging techniques and their characteristics (Tamaki & Kuge, 2010)	7
Table 2.1	Abundance of naturally occurring nuclei and their gyromagnetic ratios (Cowan, 1997)	42
Table 3.1	T_1 and T_2 relaxation times of brain tissues obtained at 1.5 T and 3.0 T (Lu et al., 2005)	128
Table 3.2	T_1 and T_2 relaxation times determined from various tumor regions and contralateral white matter in three tumor types (Badve et al., 2017)	129
Table 4.1	NMR transverse magnetized RFIDs and velocities for different tissues and parameter $a = 1$, $x = 0.001$ at $n = 1, 2, 3, 4, 5$	166
Table 4.2	NMR transverse magnetized RFIDs and velocities for different tissues and parameter $a = 5$, $x = 0.001$ at $n = 1, 2, 3, 4, 5$	168
Table 4.3	NMR transverse magnetized RF IDs and velocities for different tissues and parameter $a = 10$, $x = 0.001$ at $n = 1, 2, 3, 4, 5$	169
Table 4.4	Table of NMR transverse magnetized RFIDs and velocities for different tissues and parameter $a = 15$, $x = 0.001$ at $n = 1, 2, 3, 4, 5$	170
Table 4.5	NMR transverse magnetized RFIDs and velocities for different tissues and parameter $a = 20$, $x = 0.001$ at $n = 1, 2, 3, 4, 5$	171
Table 4.6	NMR transverse magnetized RF IDs and velocities for different tissues and parameter $a = 25$, $x = 0.001$ at $n = 1, 2, 3, 4, 5$	172
Table 4.7	Table of NMR transverse magnetized RF IDs and velocities for different tissues and parameter $a = 50$, $x = 0.001$ at $n = 1, 2, 3, 4, 5$	173

Table 4.8	NMR transverse magnetized RF IDs and velocities for different tissues and parameter $a = 0.1$, $x = 0.001$ at $n = 1, 2, 3, 4, 5$	174
Table 4.9	NMR transverse magnetized RF IDs and velocities for different tissues and parameter $a = 0.01$, $x = 0.001$ at $n = 1, 2, 3, 4, 5$	175
Table 4.10	NMR transverse magnetized RF IDs and velocities for different tissues and parameter $a = 0.001$, $x = 0.001$ at $n = 1, 2, 3, 4, 5$	176
Table 4.11	NMR transverse magnetized RF IDs and velocities for different tissues and parameter $a = 0.001$, $x = 0.001$ at $n = 1, 2, 3, 4, 5$	177
Table 5.1	Mean values of T_1 and T_2 from solid tumor regions in three tumor types scanned at $B_0 = 3.0$ T and radiofrequency pulse duration of $800 \mu\text{s}$	183
Table 5.2	Magnetic resonance signal dataset calculated from MR fingerprinting measurements and Eq. (5.10)	184
Table 5.3	Magnetic resonance signal dataset calculated from MR fingerprinting measurements and Eq. (5.11)	195
Table 5.4	Classification accuracies of different machine learning models from the datasets of Tables 5.2 and 5.3	217
Table 6.1	Spectroscopic notations and quantum states	235
Table 6.2	Relaxation rates of human cytochrome C	238
Table 6.3	Parameters used for simulations of Yukawa potential formulation and Coulomb potential formulation	238
Table 7.1	Hemodynamic properties of human blood vessels	253
Table 8.1	Dataset of NMR relaxometry for three classes of brain tumor (glioblastoma multiforme, metastasis and lower grade glioma)	277
Table 8.2	Statistical summary of NMR relaxometry dataset	281
Table 8.3	Accuracy of the models	284
Table 8.4	Cohen's Kappa obtained for the models	284
Table 8.5	Summary of the results of LDA	285
Table 8.6	Confusion matrix of the LDA model	286
Table 8.7	Overall performance statistics of the LDA model	286
Table 8.8	Performance statistics of the LDA model according to tumour type	286
Table 9.1	Numerical data extracted from necrosis image	300
Table 9.2	Numerical data extracted from tumor image	302
Table 9.3	Filtered extracted numerical data from the necrosis image	311
Table 9.4	Filtered extracted numerical data from the tumor image	311
Table 10.1	NMR relaxometric properties of four contrast agents (Rohrer et al., 2005) in three physiological environments (PE)	320

Table 10.2	NMR relaxivities of investigated contrast three solvents at $B_0 = 1.5$ T	328
Table 10.3	A cross view of the r_1 relaxivity dataset	329
Table 10.4	A cross view of the r_2 relaxivity dataset	330
Table 10.5	Statistical summary of the r_1 relaxivity dataset	331
Table 10.6	Statistical summary of the r_2 relaxivity dataset	332
Table 10.7	Performance of XGBClassifier on the dataset	336

Book Review

This book presents mathematical and computational concepts that can be applied to the analysis of brain tissues, to complement noninvasive imaging for efficient and early diagnosis of disease. The basis of these concepts is the Bloch NMR flow equations.

Chapter 1 establishes the biological bases of disease and the need for early diagnosis for prompt intervention. It highlights the drawbacks of invasive medical procedures which include tissue damage and false diagnosis. In Chap. 2, the authors describe how magnetic resonance works and how knowledge of the expected behavior of normal tissue helps to determine the presence of disease when abnormal behavior is noticed. Specifically, it describes the principles and physics of magnetic resonance imaging (MRI), the design of MRI equipment, and how images are acquired and enhanced for analysis. Then it goes on to show how Bloch's flow equations can mathematically model MRIs of different disease conditions. Chapter 3 presents a new mathematical formulation for diffusion MRI developed by solving the Bloch NMR flow equation. This would probably be the most opaque chapter for people without a strong grounding in physics and mathematics, but will be interesting to diffusion MRI specialists.

In Chap. 4, the Bloch NMR flow equation is developed into two second-order differential equations which can predict fluid flow at suction points analytically and precisely. The flow properties of the time-independent Bloch NMR flow equations describe the dynamics of blood flow under the influence of a radio frequency identification (RFID) system subject to the resonance condition at Larmor frequency. These equations depend on existing knowledge of fluid dynamics applied to predict analytically and precisely the blood flow behavior at suction points in the circulatory system.

Chapter 5 presents practical ways of using computational MRI to provide innovative data-driven algorithms to predict, simplify, and characterize brain tumors and delineate their mechanisms. The chapter first establishes the inadequacies of current imaging techniques to differentiate between primary and metastatic malignant brain tumors for better treatment planning. To address the problem, the chapter presents a computational MR model developed from Bloch's NMR flow equation to classify

brain tumors using MRF-derived relaxometric data. The performance of eight machine learning models as diagnostic tools was assessed. Developments in computational MRI could lead to the invention of interactive brain tumor classification apps and the design/development of wearable devices in the future.

Chapter 6 focuses on quantum and classical mechanical analyses of the Yukawa potential which is based on a differential equation developed from Bloch's NMR flow equations, with the wave function of hydrogen atoms and hydrogen-like ions being represented in terms of NMR parameters. As a method of analyzing hydrogen atom and hydrogen-like ions, three advantages put this model above others: its easier visualization, being based on the analytical solution of the fundamental Bloch NMR flow equations, the formulation of a weighting parameter as an interesting physical mechanism that provides a switch between classical and quantum mechanism, and the combination of the quantum and the classical models which can complement each other to provide an excellent innovation for the NMR study of atomic structure of hydrogen-like particles in general for patient-specific and time-unique solutions, an important aspect of personalized medicine. This would pave the way for the next generation of molecular medicine.

While previous chapters focused on solid tissue, Chap. 7 focuses on the flow of blood and presents methods of applying known quantum mechanical formulations and models to the Bloch NMR flow equations, providing a theoretical foundation that may enhance accurate understanding of the transport of nanodevices in microscopic blood vessels used in nanomedicine. Nanomachines can be developed to deliver specially designed quantum drugs carried by blood to the site of infections. The question is: "how much is known of how blood flows to these sites and how to exercise control over the nanomachines carrying the drugs?" The chapter answers these questions by presenting a mathematical algorithm to describe in detail the dynamical state of the hydrogen atom starting from the NMR flow equation, using basic quantum mechanical tools. The mathematical approach may be applied to any situation of restricted fluid flow in small blood vessels.

The premise of Chap. 8 is that experimental methods must be complemented by developing appropriate mathematical models and innovative computer simulation for efficient diagnosis. One method applied in the chapter is the use of R machine learning, which can be used for intensity visualization, intensity separation, and neighborhood information. The works of different researchers in the areas of noise removal and image enhancement were reviewed. Then, an algorithm to classify human brain tumors hierarchically is presented. Using R machine language with various classifiers, distinctions are made between glioblastoma multiforme, metastasis, and lower grade glioma. Chapter 9 demonstrates the use of Avizo, an imaging processing software for distinguishing between radiation necrosis and tumor progression. By the use of several computer images generated by the software, the differences between necrosis and tumor images are established.

Chapter 10 provides a detailed discussion of MR contrast agents GADOVIST, MULTIHANCE, and Gadomer, and their physicochemical basis, which had been previously mentioned in Chap. 2. For the various contrast agents, a Wolfram Mathematica computer program successfully distinguished between the

performances of the different MR contrast agents. Solutions to the time-independent NMR Bloch flow equation feature in the writing of the computer program, and the magnetization power of various contrast agents within various laboratory solvents or human tissues was compared quite easily. This can prepare the reader for future innovations in computational MRI.

Chapter 11 briefly highlights the overall goal of the book, especially to facilitate innovation in advanced MRI technologies that could be applied to fundamental basic and preclinical research problems in neuro-oncology and to develop training software that can simulate MRI experiments and provide visual training tools to help understand MRI technology. These might provide support for the development, maintenance, and operation of appropriate MRI devices.

The book will make an interesting read for its audience. The language is accessible, and the equations provide detailed and step-by-step procedures of the mathematical developments for the readers.

Federal University of Technology,
Akure, Nigeria

Funmi O. Olubode-Sawe